J|A|C|S
ARTICLES
Published on Web 03/23/2006

Electronic and Molecular Structure of Photoexcited $[Ru^{II}(bpy)_3]^{2+}$ Probed by Picosecond X-ray Absorption Spectroscopy

Wojciech Gawelda,[†,‡] Melanie Johnson,[†,‡] Frank M. F. de Groot,[§] Rafael Abela,[‡] Christian Bressler,[†] and Majed Chergui*[,†]

Contribution from the Ecole Polytechnique Fédérale de Lausanne, Laboratoire de Spectroscopie Ultrarapide, Institut des Sciences et Ingénierie Chimiques, CH-1015 Lausanne-Dorigny, Switzerland, Swiss Light Source, Paul Scherrer Institut, CH-5232 Villigen PSI, Switzerland, and Department of Inorganic Chemistry and Catalysis, Utrecht University, Sorbonnelaan 16, 3584 CA Utrecht, The Netherlands

Received July 22, 2005; E-mail: majed.chergui@epfl.ch

Abstract: $L_{2,3}$ X-ray absorption spectra of aqueous $[Ru^{II}(bpy)_3]^{2+}$ have been recorded in its ground and excited states, 50 ps after short pulse laser excitation. Significant changes in both the XANES (X-ray Near-Edge Absorption Structure) and the EXAFS (Extended X-ray Absorption Fine Structure) regions of the excited state complex are detected. The XANES line shapes have been quantitatively simulated using a crystal field multiplet code in trigonal symmetry. In addition, spectral changes in the EXAFS region of both ground and excited states are analyzed in order to extract structural parameters of their corresponding molecular structures. We obtain a Ru−N bond contraction by ∼0.03 Å in the excited-state complex, as compared to the ground-state compound. This contraction results from electrostatic and polarization contributions, limited by steric constraints on the bpy ligands.

1. Introduction

Ruthenium(II)-tris-2,2′-bipyridine, ($[Ru^{II}(bpy)_3]^{2+}$), represents a paradigm[1] and a model system of intramolecular electron-transfer reactions.[2] It is also the core member of a family of transition metal-based devices for solar energy conversion.[3−7] $[Ru^{II}(bpy)_3]^{2+}$ has been extensively studied, and most is known about its excited-state properties.[1,5,8−10] The photochemical cycle of $[Ru^{II}(bpy)_3]^{2+}$ can be sketched by a simple level scheme (Figure 1). Light excitation of a metal-centered valence electron from its singlet ground state (^{1}GS) (originating from the ligand-field split 4d level) into the lowest-energy absorption band (400−500 nm) leads to the formation of a Franck−Condon singlet Metal-to-Ligand Charge Transfer (^{1}MLCT) state and localization of the electron on one of the bipyridine ligands, which undergoes intersystem crossing to a long-lived triplet state (^{3}MLCT) in less than 300 fs:[11,12]

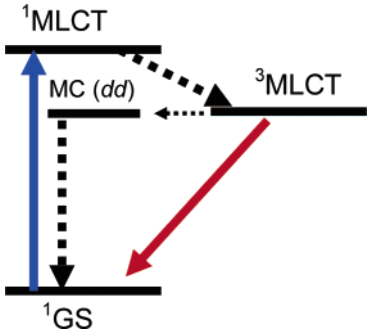

Figure 1. Photochemical cycle of $[Ru^{II}(bpy)_3]^{2+}$ in a simplified energy level scheme. Absorption of visible light removes a metal-centered (MC) 4d electron in its singlet ground state (^{1}GS) into the singlet Metal-to-Ligand Charge Transfer (^{1}MLCT) state, where it undergoes ultrafast intersystem crossing into the triplet ^{3}MLCT state, localized onto the bipyridine ligand system. The ^{3}MLCT state decays nonradiatively via the high vibrational levels of the MC ground state and via excited states[1] and radiatively with a fluorescence lifetime of ∼600 ns at room temperature.

$$[Ru^{II}(bpy)_3]^{2+}\ (^1GS) + h\nu \rightarrow [Ru^{III}(bpy^{-1/3})_3]^{2+}\ (^1MLCT) \rightarrow [Ru^{III}(bpy^{-1})(bpy)_2]^{2+}\ (^3MLCT) \quad (1)$$

At room temperature and in aqueous solutions the emission of

[†] Ecole Polytechnique Fédérale de Lausanne.
[‡] Paul Scherrer Institut.
[§] Utrecht University.

(1) Juris, A.; Balzani, V.; Barigelletti, F.; Campagna, S.; Belser, P.; Von-zelewsky, A. *Coord. Chem. Rev.* **1988**, *84*, 85−277.
(2) Gray, H. B. In *Electron transfer in chemistry*; Balzani, V., Ed.; Wiley-VCH: Weinheim, 2001.
(3) Kalyanasundaram, K. *Coord. Chem. Rev.* **1982**, *46*, 159−244.
(4) Sauvage, J. P.; Collin, J. P.; Chambron, J. C.; Guillerez, S.; Coudret, C.; Balzani, V.; Barigelletti, F.; Decola, L.; Flamigni, L. *Chem. Rev.* **1994**, *94*, 993−1019.
(5) Balzani, V.; Sabbatini, N.; Scandola, F. *Chem. Rev.* **1986**, *86*, 319−337.
(6) Kalyanasundaram, K.; Gratzel, M. *Coord. Chem. Rev.* **1998**, *177*, 347−414.
(7) Kalyanasundaram, K.; Zakeeruddin, S. M.; Nazeeruddin, M. K. *Coord. Chem. Rev.* **1994**, *94*, 259−264.
(8) Balzani, V.; Juris, A.; Venturi, M.; Campagna, S.; Serroni, S. *Chem. Rev.* **1996**, *96*, 759−833.
(9) Vlcek, A. *Coord. Chem. Rev.* **1998**, *177*, 1−2.
(10) Vlcek, A. *Coord. Chem. Rev.* **2000**, *200*, 933−977.
(11) Damrauer, N. H.; Cerullo, G.; Yeh, A.; Boussie, T. R.; Shank, C. V.; McCusker, J. K. *Science* **1997**, *275*, 54−57.
(12) Yeh, A. T.; Shank, C. V.; McCusker, J. K. *Science* **2000**, *289*, 935−938.

the ^{3}MLCT state exhibits a measured lifetime of about 600 ns[13] due to efficient (95%) nonradiative quenching to high vibrational levels of the ground state and to the triplet Metal-Centered (MC) states[1] (Figure 1).

The photoinduced electronic changes (change of oxidation state, localization of the electron on a ligand) should have consequences on the molecular structure. The localization of the electron on one bpy ligand changes the ground state D_3 symmetry to a C_2 symmetry in the ^{3}MLCT state, at least from the electronic point of view and, probably, the structural one also. Both the increased electrostatic interaction and polarization between the Ru^{III} atom and the bpy^- and bpy ligands, as well as the reduced π-back-bonding, due to the increased oxidation state of the Ru atom, should lead to a modification of the Ru−N bond distances.

The interplay between electronic and geometric changes is of prime importance in elementary charge-transfer processes. From a fundamental point of view, structural information is valuable in order to get insight into the photocycle itself and the nonadiabatic dynamics therein taking place. From a practical point of view, this may help design new transition-metal-based compounds for optimum reductive−oxidative functions with applications in solar cells. Structural information is of special interest in the development of molecular-based materials, capable of performing efficient intermolecular charge transfer, by means of a control of the spatial arrangement of their constituents.[14,15] In several such arrangements strong electronic coupling between the excited species and its nearest neighbors makes the electron transfer adiabatic.[10] Hence, the rate is governed by the nuclear dynamics, as the activation energy depends to a great extent on the reorganization energy of the reacting species prior to electron transfer, which involves the stretching or contraction of metal−ligand bonds.

Despite the fundamental and practical importance of metal−polypyridine (and in particular Ru-) complexes and the numerous studies that were undertaken on these systems,[13,5−11,13,16] surprisingly few studies have addressed the issue of the structural changes occurring upon photoexcitation. Static and time-resolved resonance Raman studies have been carried out on $[Ru^{II}(bpy)_3]^{2+}$ to measure the structural changes in the ^{3}MLCT photoproduct,[17−20] but these have mainly concentrated on the bond changes within the bpy^- ligand. In only one work has an estimate of the Ru−N bond change (0.048 Å) been given, namely for the $[Ru^{II}(NH_3)_4(bpy)]^{2+}$ complex, using a time-dependent treatment of the preresonance Raman spectrum.[17] However, with these optical methods it is difficult to detect the low frequency modes, which are precisely those of interest for assessing the metal−ligand bond length changes. While crystallographic studies on $[Ru^{II}(bpy)_3]^{2+}$ and $[Ru^{III}(bpy)_3]^{3+}$ showed no difference in the Ru−N distance between both compounds,[21] similar studies on $[Ru^{II}(NH_3)_6]^{2+}$ and $[Ru^{III}(NH_3)_6]^{3+}$ pointed to a bond contraction of ca. −0.04 Å for the trivalent Ru center,[22] which was attributed to polarization effects[21,22] due to the increased charge of the central Ru ion. However, these experiments are difficult to compare with photoexcited Ru−polypyridine complexes (in particular, $[Ru^{II}(bpy)_3]^{2+}$), as the photocycle of the latter implies a change of charge and spin along with the reduction of the ligand.

X-ray Absorption Spectroscopy (XAS) is a direct approach to determine the molecular structure changes and the electronic ones that underlie them. In a laser pump/X-ray probe scheme, it can thus deliver information about the transient electronic structure changes including orbital occupancy, degree of oxidation, and ligand field strength in the valence states (which are those driving chemical reactions), via XANES spectroscopy. Simultaneously, coordination numbers and bond distances around a specific atom (here, the Ru atom) can be reliably determined from the EXAFS spectroscopy.[23]

The goal of the present work is to provide a detailed analysis of the electronic and molecular structure of the ground and excited states of $[Ru^{II}(bpy)_3]^{2+}$ via static and picosecond-resolved XANES and EXAFS. The rationale behind this approach has been extensively discussed in ref 23.

So far, few successful time-resolved XAS studies have been reported (see ref 23 for a detailed review), let alone of coordination compounds in the liquid phase. Chen and co-workers investigated photoexcited NiTPP (TPP = tetraphenylporphyrin) by XANES and EXAFS, with a resolution of 14 ns, using X-ray pulses from a synchrotron,[24] and a Cu−diimine complex with 100 ps X-ray pulses.[25] These studies were aimed at understanding the coordination of solvent species to the excited complex. In a foregoing contribution, we showed that we can capture the ^{3}MLCT of $[Ru^{II}(bpy)_3]^{2+}$ by L_3-edge XANES of Ru at a time delay of 70 ps after laser excitation.[26]

In this contribution, we present the first complete picosecond resolved XANES and EXAFS study of a Ru−polypyridine compound ($[Ru^{II}(bpy)_3]^{2+}$) at both L_3- and L_2-edges of the metal atom. The experimental procedures are given in the Supporting Information and in refs 27−29. We present a detailed analysis of the XANES at both *L*-edges of Ru, based on a calculation of the transition energies and intensities of the core excitations, which provides information about the ligand field of the excited complex and about the bond distances, fully supported by our analysis of the EXAFS, and we find that the Ru−N distances actually *decrease* in the excited state. The origin of this change and its implications for electron-transfer processes are also discussed.

(13) Creutz, C.; Chou, M.; Netzel, T. L.; Okumura, M.; Sutin, N. *J. Am. Chem. Soc.* **1980**, *102*, 1309−1319.
(14) Fleming, C. N.; Maxwell, K. A.; DeSimone, J. M.; Meyer, T. J.; Papanikolas, J. M. *J. Am. Chem. Soc.* **2001**, *123*, 10336−10347.
(15) Shaw, G. B.; Papanikolas, J. M. *J. Phys. Chem. B* **2002**, *106*, 6156−6162.
(16) Calzaferri, G.; Rytz, R. *J. Phys. Chem.* **1995**, *99*, 12141−12150.
(17) Doorn, S. K.; Hupp, J. T. *J. Am. Chem. Soc.* **1989**, *111*, 4704−4712.
(18) Mallick, P. K.; Strommen, D. P.; Kincaid, J. R. *J. Am. Chem. Soc.* **1990**, *112*, 1686−1690.
(19) Strommen, D. P.; Mallick, P. K.; Danzer, G. D.; Lumpkin, R. S.; Kincaid, J. R. *J. Phys. Chem.* **1990**, *94*, 1357−1366.
(20) Baranovski, V. I.; Lubimova, O. O.; Makarov, A. A.; Sizova, O. V. *Chem. Phys. Lett.* **2002**, *361*, 196−202.
(21) Biner, M.; Bürgi, H. B.; Ludi, A.; Röhr, C. *J. Am. Chem. Soc.* **1992**, *114*, 5197−5203.
(22) Stynes, H. C.; Ibers, J. A. *Inorg. Chem.* **1971**, *10*, 2304−2308.
(23) Bressler, C.; Chergui, M. *Chem. Rev.* **2004**, *104*, 1781−1812.
(24) Chen, L. X.; Jager, W. J. H.; Jennings, G.; Gosztola, D. J.; Munkholm, A.; Hessler, J. P. *Science* **2001**, *292*, 262−264.
(25) Chen, L. X.; Jennings, G.; Liu, T.; Gosztola, D. J.; Hessler, J. P.; Scaltrito, D. V.; Meyer, G. J. *J. Am. Chem. Soc.* **2002**, *124*, 10861−10867.
(26) Saes, M.; Bressler, C.; Abela, R.; Grolimund, D.; Johnson, S. L.; Heimann, P. A.; Chergui, M. *Phys. Rev. Lett.* **2003**, *90*, 047403−047401.
(27) Saes, M. G. W.; Kaiser, M.; Tarnovsky, A.; Bressler, Ch.; Chergui, M.; Johnson, S. L.; Grolimund, D.; Abela, R. *Synchrotron Radiation News* **2003**, *16*, 12.
(28) Saes, M.; Bressler, C.; van Mourik, F.; Gawelda, W.; Kaiser, M.; Chergui, M.; Bressler, C.; Grolimund, D.; Abela, R.; Glover, T. E.; Heimann, P. A.; Schoenlein, R. W.; Johnson, S. L.; Lindenberg, A. M.; Falcone, R. W. *Rev. Sci. Instrum.* **2004**, *75*, 24−30.
(29) Gawelda, W.; Bressler, C.; Saes, M.; Kaiser, M.; Tarnovsky, A.; Grolimund, D.; Johnson, S. L.; Abela, R.; Chergui, M. *Physica Scripta* **2005**, *T115*, 102.

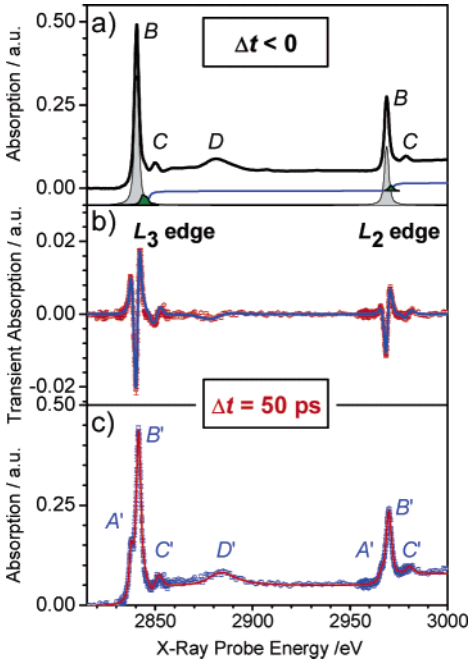

Figure 2. (a) Static absorption spectrum of aqueous $[Ru(bpy)_3]^{2+}$ in the region of the Ru L_3- and L_2-edges (solid black trace with labels) together with the fit results to features B (gray bands), higher-lying bound-bound transitions (green bands), and the edge step of the ionization continuum (solid blue curve). See text and Table 1 for details. (b) Transient difference absorption spectrum measured 50 ps after photoexcitation. The solid line results from the a global fit of the spectrum (Table 1). (c) Excited-state XAS spectrum extracted from spectra a and b using eq 2. The red trace represents the results of the fit (as in spectrum a), with the parameters given in Table 1. Note that compared to spectrum a, an additional band (A′) shows up.

2. Results

The static XAS spectrum of the ground-state complex, recorded under pump−probe conditions, is shown in Figure 2a. It exhibits bands labeled B, C, and D at both L-edges, which we assign below. Figure 2b shows the difference spectrum between the unexcited ($\Delta t < 0$) and the excited sample transmission spectra, at a time delay of 50 ps after laser excitation. Although the X-ray pulse width is 70 ps, this time delay is determined by the low jitter between laser and X-ray pulses.[29,27]

Figure 3 compares the difference absorption spectra at time delays of 50 ps and 70 ns, where the latter has been multiplied by 4.8 to match the 50 ps spectrum. This scaling is motivated by the temporal evolution of the changes observed near the B-band (see Figure S1). To within noise (see residual in Figure 3), the spectra are identical at both time delays and the essential features remain unchanged over time, in particular the weak changes in the region of the D-band. This demonstrates that the changes in the regions of the A/B features and the D-band go hand in hand. This point is of importance for the interpretation of the structural analysis, since features A/B are of electronic nature, while D is geometric (see below).

We attribute the changes observed in Figures 2b and 3 predominantly to the ^{3}MLCT photoproduct, for the following reasons:

(a) In ref 27, we showed that, for a low concentration sample ($c = 10$ mM), the decay kinetics of the X-ray signal at the B feature reflects that of the simultaneously recorded ^{3}MLCT phosphorescence. This is evidence that the kinetics of the X-ray

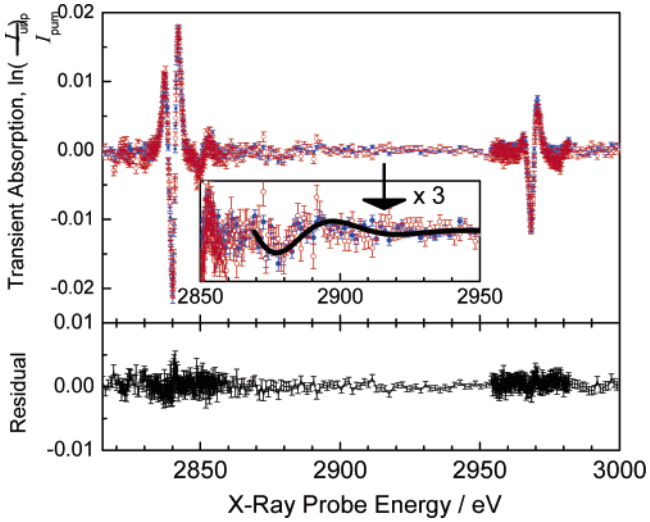

Figure 3. Comparison of the difference absorption spectra at 50 ps (red) and 70 ns (blue) time delay, with the 70 ns transient having been multiplied by 4.8 (see Figure S1). The residual difference between both transients is given below, while the inset shows a zoom of the EXAFS region (together with the transient difference EXAFS from the FEFF simulation). Note the identical signals in the region of the D feature near 2880 eV (also seen in the residual).

signal reflects that of the ^{3}MLCT state. In the present case ($c = 80$ mM), the laser penetration depth is 10−20 μm of the 0.1 mm liquid jet, and it therefore deposits more energy into this layer, thus heating this part of the sample with a radial distribution of temperatures along the Gaussian-shaped excitation pulse. Microscopic imaging of the phosphorescence from the center outward shows different decay traces with increasing time constants toward the outer edges of the Gaussian pump area. The phosphorescence decay curve near the center nicely matches that of the X-ray decay signal, since the tighter X-ray spot also only samples the central region of excitation. The observed temperature-dependent decay is fully in line with the temperature-dependent intramolecular quenching of aqueous $[Ru(bpy)_3]^*$ in its ^{3}MLCT state. We can therefore safely conclude that the transient X-ray signal is predominantly due to the ^{3}MLCT state.

(b) Intense laser excitation, as used in this study, leads also to the fully ionized complex $[Ru^{III}(bpy)_3]^{3+}$ and to the reduced species $[Ru^{II}(bpy)_2(bpy)^-]^{1+}$ (following recombination with photogenerated solvated electrons), along with the ^{3}MLCT state. We have quantitatively determined the concentrations of these three product species in laser-only studies (not shown here) in the 1−20 mM range (higher concentrations are optically inaccessible due to total absorption of the 0.1 mm sample) and found that, in all cases, the ^{3}MLCT state is to $>^2/_3$ the dominant product species in the 10−100 ps time range. In addition, the concentration of the ionized species $[Ru^{III}(bpy)_3]^{3+}$ decreases to below our detection sensitivity after a few nanoseconds, leaving only the reduced species and the dominant ^{3}MLCT state (now to >80%) in the laser excited solution. Therefore, we can expect that, after 70 ns, we are left with only those two species. In addition, as far as changes in the region of the D-band (which is an EXAFS feature) are concerned, we believe that $[Ru^{III}(bpy)_3]^{3+}$ does not contribute because X-ray diffraction studies of $[Ru^{II}(bpy)_3]^{2+}$ and $[Ru^{III}(bpy)_3]^{3+}$ [21] point to no structural changes (which would cause the changes in the region of the D-band) between both compounds. Last, the correspondence

Table 1. Energies (*E*) and Full Width at Half Maximum (Γ) of the Spectral Features Appearing in the XAS Spectra of the Ground State (GS) and Excited State (GS) Complex Obtained from the Fit of Figures 2a, 2c and 4[a]

		4d (t_{2g}), A		4d (e_g), B		C		D		additional transitions		IP
		E	Γ	*E*	Γ	*E*	Γ	*E*	Γ	*E*	Γ	*E*
GS	L_3			2840.5	2.7	2850.0	3.3	2881.1	16.7	2843.5	2.6	2846.8
										2845.6	2.6	
	L_2			2968.8	2.7	2978.7	4.0			2971.0	2.7	2972.2
ES	L_3	2837.6	2.5	2841.4	3.0	2852.0	3.3	2883.9	15.8	2844.4	2.6	2848.6
										2846.6	2.6	
	L_2	2966.0	2.7	2969.8	3.1	2980.6	4.3			2972.0	2.7	2974.1

[a] The ionization potential (IP) is taken as the energy at the center of the step function (see text for details). The additional transitions correspond to the weak green bands found above the B-bands in Figure 2. All units are in eV. Uncertainty 0.1 eV for L_3-edge, 0.1−0.2 eV for L_2-edge.

between the signals at the D- and B-bands (Figure 3) confirms the minor role of the oxidized complex in the X-ray difference spectra. The relative population between reduced and ^{3}MLCT species will also change considerably between 50 ps and 70 ns (favoring the reduced species at longer time delays). Since we do not observe a significant change in the difference XAS between both time delays (Figure 3) we can safely assume that we are mainly dealing with XAS changes due to the desired ^{3}MLCT product state.

Thus, all evidence points to the fact that our X-ray signal in the picosecond to the nanosecond time domain (Figures 2 to 4) is largely dominated by the ^{3}MLCT photoproduct. We therefore constructed the XAS spectrum of the photoproduct via[23]

$$T(E,t) = f(t) \cdot [A_{es}(E,t) - A_{gs}(E)] \qquad (2)$$

where $f(t)$ is the relative population of the excited complex species (^{3}MLCT) at time t, and $T(E,t)$ denotes the transient difference absorption spectrum (Figure 2b), which contains all the photoinduced changes from the ground-state complex spectrum, $A_{gs}(E)$ (Figure 2a), to the excited complex spectrum, $A_{es}(E,t)$, at the time t following photoexcitation. The time-dependent photolysis yield, $f(t)$, has an influence on the spectral shape of the excited-state XAS $A_{es}(E,t)$, and we measured it independently in laser-only transient absorption experiments under identical experimental conditions (concentration, sample geometry, pump power) and obtained $f(t) \cong 10\%$. Figure 2c shows the recovered X-ray absorption spectrum of the photo-excited species, where we distinguish bands labeled B′, C′, and D′, that are counterparts of the bands in the ground-state spectrum (hereafter primes will always be used for the excited compound spectral features), while an additional spectral feature (A′) shows up at both *L*-edges.

For a more detailed analysis of the data, we require accurate information about the individual peak positions and widths and about the energy of the ionization potential (IP). For this purpose we performed a least-squares global fit of the entire spectra in Figures 2a and 2c. We used Voigt profiles for the A′ and B/B′ features, an arctangent step function for the IP, and an asymmetric Voigt profile for both features C/C′ and D/D′ (decomposed bands not shown). In addition, thanks to our sensitivity, we identify transitions lying at higher energies, which we fitted with Voigt profiles (two for the L_3- and one for the L_2-edge), and these are seen as green bands in Figure 2a. The Lorentzian widths for all Voigt profiles and the edge step functions were fixed to the lifetime width of the L-edges of Ru, which amounts to 1.75 eV for the L_3-edge and between

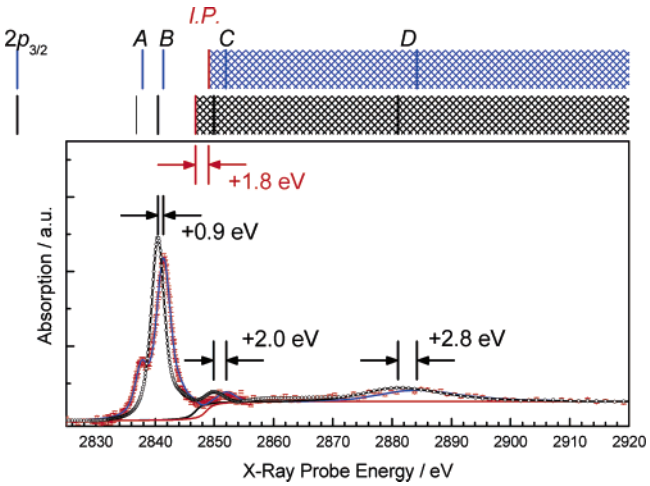

Figure 4. Ground (black dots) and excited state (red dots with errors bars) XAS spectra of $[Ru(bpy)_3]^{2+}$ at the Ru L_3-edge, together with a fit of the dominant features (solid curve through data points). The hatched areas at the top of the figure represent the ionization threshold (IP) and continuum of the ground (black) and excited complex (blue). The measured energetic positions of the various spectral features (bands and ionization edge) are indicated above the spectrum and are given in Table 1.

1.9 and 2.1 eV in the case of the L_2-edge,[30,31] while the Gaussian widths were fitted and delivered results in the 1.2−1.4 eV range, as expected from the calculated monochromator width (energy resolution) at these X-ray energies.[28] The fit results are summarized in Table 1.

In addition, Figure 4 zooms into details of the ground and excited state (time delay: 50 ps) L_3-edge absorption spectra, along with the resulting fit curves, showing the very good agreement with the experiment. The *B*′ peaks at both L_3- and L_2-edges have shifted to the blue by 0.9 eV with respect to the B peaks. This shift results from the change of oxidation state of the Ru atom, in good agreement with the difference observed between ruthenium compounds of different valencies previously reported.[32−34] It is also fully in line with the fact that an entire charge is transferred to the bpy ligand, as supported by quantum chemical calculations.[16,35] It is important to stress not only the accuracy of the fits concerning the peak positions (<0.1 eV) but also the precise determination of the oxidation-state induced shift of the ionization potential of 1.8 eV (Table 1). This is

(30) de Siervo, A.; Landers, R.; de Castro, S. G. C.; Kleiman, G. G. *J. Electron Spectrosc.* **1998**, *88*, 429−433.
(31) Ohno, M.; van Riessen, G. A. *J. Electron. Spectrosc.* **2003**, *128*, 1−31.
(32) Sham, T. K. *J. Am. Chem. Soc.* **1983**, *105*, 2269−2273.
(33) Sugiura, C.; Kitamura, M.; Muramatsu, S. *J. Chem. Phys.* **1986**, *84*, 4824−4827.
(34) Sham, T. K. *J. Chem. Phys.* **1985**, *83*, 3222−3224.
(35) Buchs, M.; Daul, C. *Chimia* **1998**, *52*, 163−166.

crucial for a precise EXAFS analysis as will be discussed in section 3.3.

3. Analysis and Discussion

3.1. Ground and Excited Compound X-ray Absorption Spectra. The spectra in Figures 2 to 4 are the first complete L_3- and L_2-edge XAFS spectra of a Ru−polypyridine complex ($[Ru^{II}(bpy)_3]^{2+}$) in its ground and its excited state, captured picoseconds onward after photoexcitation. Before discussing the photoinduced changes, we recall the origin of the bound−bound transitions. The Ru atom has a $4d^6$ configuration in the ground state of $[Ru^{II}(bpy)_3]^{2+}$, and in the presence of an octahedral crystal field the 4d orbitals transform into t_{2g} and e_g orbitals, separated in energy by the octahedral crystal field splitting energy (denoted as 10Dq [36]). Since we are dealing with a low spin compound, all 6 electrons fill up the t_{2g} orbitals, while the e_g orbitals are empty. This defines the ground state with $^1A_1$ symmetry. Note that this $^1A_1$ ground state is not affected by the trigonal distortion or by the 4d spin−orbit coupling ζLS. The L-edges arise from atomiclike electric dipole transitions (change of angular momentum $\Delta l = \pm 1$) from the $2p_{1/2}$ (L_2) and $2p_{3/2}$ (L_3) core orbitals to unoccupied orbitals of both s and d symmetry. Excitation of the 2p electron is only possible to the empty e_g states, giving rise to the B-band at both L_3- and L_2-edges. In trivalent compounds, such as $[Ru^{III}(NH_3)_6]^{3+}$, an additional A-band appears ~3.93 eV below the B-band at the L_3 edge but not at the L_2-edge, since an electron is missing in the t_{2g} orbital.[32] The A−B splitting therefore delivers information on the ligand field splitting. Likewise, the new feature A′, seen in Figures 2c and 4, originates from the light-driven charge-transfer process (changing the central atom occupancy from $4d^6$ to $4d^5$), which creates a vacancy in the previously fully occupied t_{2g} orbital. The A′−B′ splitting amounts to 3.75 eV, which is close to the value found in purely octahedral compounds,[32] suggesting that the trigonal distortion (D_3) and the axial distortion (leading to C_2 symmetry) of the photoexcited complex are minor perturbations to the dominant O_h ligand field.

While the XAS spectra of the trivalent and octahedral compounds $[Ru^{III}(NH_3)_6]^{3+}$ and $[Ru^{III}Cl_6]^{3-}$ do not exhibit the A′(t_{2g}) feature at the L_2-edge,[32−34] it does show up at the L_2-edge of the photogenerated $[Ru^{III}(bpy)_2bpy^-]^{2+}$. To explain this difference, we have to analyze the symmetries of the $2p^64d^5$ initial and the $2p^54d^6$ final states of the X-ray transition of the laser-excited compound, in the field of the ligands. In the case of octahedral compounds, the $4d^5$ initial state has $^2T_2$ symmetry. Spin−orbit coupling is important, which implies that the double group symmetry is given by the multiplication of the spin (E′) and the orbital (T_2) symmetries. This gives the double group symmetries Γ_7 and Γ_8, where the initial state is given by Γ_7.[37] The final state is $2p^5t_{2g}{}^6$ with $^2T_1$ symmetry. In double group symmetry, we have $E' \otimes T_1 = \Gamma_6 + \Gamma_8$, which is split by the large 2p spin−orbit coupling. The t_{2g} peak has Γ_8 symmetry at the L_3-edge and Γ_6 symmetry at the L_2-edge. An allowed dipole transition promotes $4d^5(\Gamma_7)$ to either a Γ_7 or Γ_8 state, while the Γ_6 state is forbidden. This implies that the A′(t_{2g}) band is not visible at the L_2-edge in octahedral symmetry. Trigonal distortion will mix the two spin−orbit split states, Γ_7 and Γ_8 of the $4d^5$ ground state. From the Γ_8 ground state all symmetries are dipole allowed, which implies that the Γ_6 state (A′-band) at the L_2-edge then becomes visible.

This qualitative explanation has two implications: (a) a D_3 symmetry for the excited compound is sufficient (but not unique) to explain the new spectral feature at the L_2-edge; (b) there is a close interplay between the 4d spin−orbit interaction and the D_3 ligand field. In section 3.2, we show that other features of the spectra are also quantitatively explained restricting ourselves to D_3 symmetry for the excited compound.

Turning now to features C and D in Figures 2 and 4, these lie clearly above the ionization potential (IP), according to Table 1. This is also confirmed by the fact that we observe the C feature for $[Ru^{II}(bpy)_3]^{2+}$ at nearly the same energy above the B-band as that in $[Ru^{III}(NH_3)_6]^{3+}$.[32] We assign the C-band to a quasi bound above-ionization resonance, 3.2 eV above the IP. Such resonances can arise from multiple scattering of the low energy outgoing photoelectron with the surrounding ligand atoms. The *D* feature, far above the IP, represents an EXAFS modulation and is analyzed in section 3.3 below. Finally, Table 1 and Figure 3 show a blue shift by 1.8 eV of the excited complex IP compared to that of the ground-state complex. This is due to the fact that following the removal of one of the 4d (t_{2g}) valence electrons the $2p_{1/2,3/2}$ core levels are more strongly bound (by 1.8 eV), while both 4d(t_{2g}) and (e_g) levels are lowered in energy by 0.9 eV. This difference is expected, since the change in electronic shielding upon charge transfer to the ligand system is more pronounced for the valence electrons than for the core ones. Indeed, the larger 1.8 eV shift for the 2p core levels is still relatively small with respect to their IPs of 2846.8 and 2972.2 eV, respectively, compared to the 0.9 shift for the 4d levels with their IPs around 10 eV.[16,35,38] This also agrees with previous studies by Wong et al.,[39] in which the oxidation state dependent energies were observed for vanadium compounds with valencies varying from 0 to +5, showing larger K-edge energy than valence energy shifts in the XAS.

3.2. Analysis of the XANES Line Shapes: XANES delivers information about ligand field splittings (which themselves are determined by the Ru−N bond distances) and about the modifications of selection rules (due to the changes in molecular symmetry), so we exploit it to extract structural information about the excited-state complex. For this purpose, we have simulated the XANES line shapes using the *Theo Thole* (TT) multiplet code[40−42] (see Supporting Information for details), which is based on the total Hamiltonian of the complex compound, consisting of the atomic Hamiltonian H_{atom} for Ru, to which an electrostatic crystal field Hamiltonian $H_{crystal}$ is added as a perturbation:

$$H_{total} = H_{atom} + H_{crystal} = H_{atom} + H_{O_h} + H_{D_3} + H_{\zeta LS} \quad (3)$$

where H_{O_h} is the octahedral crystal field contribution, H_{D_3} is the trigonal distortion, and $H_{\zeta LS}$ includes the 4d spin−orbit coupling. The atomic Hamiltonian contains terms due to the kinetic energy of the electrons, their Coulomb interaction with

(36) Sugano, S.; Tanabe, Y.; Kamimura, H. *Multiplets of transition-metal ions in crystals*; Academic Press: New York, 1970.
(37) Nielson, C. W.; Koster, G. F. *Spectroscopic coefficients of the p^n, d^n, and f^n Configurations*; MIR Press: Cambridge, 1963.
(38) Rensmo, H.; Lunell, S.; Siegbahn, H. *J. Photochem. Photobiol., A* **1998**, *114*, 117−124.
(39) Wong, J.; Lytle, F. W.; Messmer, R. P.; Maylotte, D. H. *Phys. Rev. B* **1984**, *30*, 5596−5610.
(40) de Groot, F. M. F. *J. Electron Spectrosc.* **1994**, *67*, 529−622.
(41) de Groot, F. M. F.; Vogel, J. Oxford University Press: Oxford, 2004.
(42) de Groot, F. M. F. *Coord. Chem. Rev.* **2005**, *249*, 31−63.

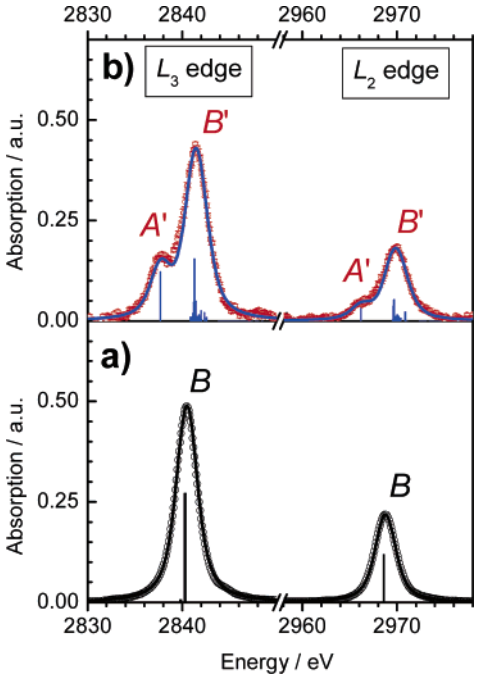

Figure 5. Experimental and simulated line shapes of the XANES L_3 and L_2 features for the ground (a) and the excited (b) complex. The calculated transition strengths for the involved energy levels are given by the stick diagram, which, after convolution with a Lorentzian (lifetime width) and Gaussian (experimental resolution), yield the solid curves. The experimental data were generated from Figure 4 after subtraction of the absorption edge and higher lying (weaker) transitions (see text). The labeled features A and B correspond to transitions to the t_{2g} and e_g levels, respectively.

the nucleus of charge +Z, their mutual electrostatic repulsion (which causes the multiplet effects), and the spin−orbit interaction of each electron.

The potential due to the ligand field is treated as a perturbation to the atomic case, and this is written as a superposition of spherical harmonics.[36] In other words, the spectra are determined by crystal field effects with splittings due to multipole 2p−4d and 4d−4d interactions, which are included in the atomic Hamiltonian. The latter are factorized in F^2 and F^4 Slater integrals, and the initial and final states are determined by the 4d−4d multipole interaction (see Table S1). Important additional interactions are caused by the core hole: the 2p core hole spin−orbit interaction splits the absorption into the L_3 and L_2 parts, and the 2p−4d multipole Coulomb and exchange interactions F^2, G^1, and G^3 (which are on the order of 1−2 eV) also modify the simulated spectrum significantly, giving rise to several spectral lines.

As mentioned above, from an electronic point of view, the excited-state structure should have a C_2 symmetry due to localization of an electron on one of the bpy ligands. The excited-state simulated XANES line shapes have been generated using the trigonal symmetry. The reasons for this choice is that the main contribution of the ligand field is the octahedral one, while the trigonal symmetry already accounts for the observation of the A′ band at the L_2-edge. Including the C_2 symmetry does not change the measured XANES of either the ground or the excited-state spectra within the (already quite high) sensitivity of the experiment.

A posteriori, the agreement between measured and the simulated XANES line shapes at both L-edges is striking (Figure 5). For this purpose, we have subtracted the IP (the edge jump) and the weaker higher-lying transitions from the experimental spectrum (step function and green bands in Figure 2a), to recover only the A′ and B′ features. The calculated transitions to the multiplet levels appear as sticks in Figure 5, and the simulated curve was derived after convolution with the Lorentzian and Gaussian functions reflecting the lifetime broadening and the experimental band-pass of the monochromator, respectively (see Supporting Information). The ground-state line shape was simulated using the literature values of the ligand field splittings (Table 2). The excellent agreement reflects the quality and precision of both the measurement and calculations.

Table 2. Ligand Field Splittings Used for the Fit of the Ground State and Excited State Complex XANES Line Shapes (Figure 5)[a]

	octahedral crystal field (10Dq)	trigonal field splitting
ground state	3.74(0.06)[b]	0.26(0.07)[c]
excited state	3.89(0.06)	0.39(0.07)

[a] All units are in eV. Uncertainties are given in brackets. [b] Reference 16. [c] Reference 59.

For the excited complex, the octahedral and trigonal field splittings were adjusted, as these parameters influence the A′−B′ splitting and intensity ratios, at both L-edges, and the widths of the A′ and B/B′ bands. Therefore the range of possible values for these parameters is very limited, and those used for the fit in Figure 5 are also given in Table 2. Here again, the agreement between experiment and simulation is remarkable, in that without the underlying multiplet structure the full line shapes cannot be retrieved. This allows us to rationalize many detailed features of the ground and excited-state spectra:

(a) The increased line width of the B′ feature with respect to the B-band (Table 1) is due to the appearance of several transitions to new sublevels of the final states. The B-band relates to a single $2p^54d^7$ final state, while the B′-band contains more than 10 $2p^54d^6$ final states spread over ∼3 eV, as indicated by the stick diagram in Figure 5.

(b) The larger line width of the B′ feature compared to A′ (Table 1) is due to a similar reason, as the excited complex t_{2g} A′-peak consists of a single transition. A similar effect was discussed by Sham for the trivalent $[Ru^{III}(NH_3)_6]^{3+}$ compound.[34]

(c) The measured intensity ratio between the B-bands at both L-edges, as well as for both ground and excited states, is very well reproduced in the simulation. These ratios are sensitive to the strength of the crystal fields and comfort us in our simplification to use a D_3 symmetry for the excited-state complex.

(d) As mentioned above, the appearance of the A′ feature at the L_2-edge is specific to the nonoctahedral trivalent excited complex. The ratio of the A′ to B′ band intensity is smaller at the L_2- compared to the L_3-edge. Since this ratio is governed by the choice of the trigonal field splitting, the excellent agreement in Figure 5 stresses its interplay with the spin−orbit interaction of the 4d electrons (see above). As a further check of this interplay, we repeated the calculations, setting the trigonal field splitting to zero, and found that the A′-band disappears at the L_2-edge, as observed for a purely octahedral compound.[32] When setting the 4d spin−orbit constant to zero, the A′-band is present at the L_2-edge, but neither the A′−B′ intensity ratios nor the ratio of B′-bands at the two L-edges is reproduced any longer. Interestingly, our excited-state XANES line shape simulation points to an increase by ∼0.13 eV of the D_3 field

splitting, compared to the ground state (Table 2). This can be related to a shorter Ru−N bond length in the case of the excited complex, although this connection is not trivial to rationalize beyond octahedral symmetry.

(e) Finally, we also calculated the transitions lying above the B-band. They are due to charge transfer (CT) effects and to higher lying (e.g., Rydberg) states. The CT satellite peaks become visible in the X-ray absorption spectra, if the final state charge transfer differs from that of the ground state.[40]

(f) The A′−B′ energy splitting is governed by the octahedral field strength 10Dq. The ligand field splitting between the t_{2g} and e_g levels, used in our simulation (Table 2), is larger for the excited state compared to the ground state (determined by quantum chemical calculations[16]).

Using an electrostatic model, König et al.[43] showed that the octahedral ligand field splitting is inversely proportional to the 5th power of the metal−ligand distance. Thus, assuming that the change of 10Dq (which is proportional to the measured change of splitting ΔE(A′−B′) between ground and excited complex) is related to a change in the Ru−N bond length,[44]

$$\frac{10Dq^{ES}}{10Dq^{GS}} = \left(\frac{R^{GS}_{Ru-N}}{R^{ES}_{Ru-N}}\right)^5 \quad (4)$$

In ref 43, this relation was found satisfied to within 2.6% for iron complexes. We used the same expression in the present case, assuming it valid for the case of Ru complexes, and calculated the photoinduced structural change of the local environment to

$$\Delta R_{Ru-N} = R^{gs}_{Ru-N}\left[\left(\frac{\Delta E_{gs}}{\Delta E_{es}}\right)^{1/5} - 1\right] \quad (5)$$

The calculated values of ΔE_{gs} for a trigonally distorted octahedron for the ground-state complex[16,35,38] and our values determined from the multiplet calculation for the excited state (Table 2), thus, deliver a contraction of the Ru−N bond by about ∼0.02 Å in the excited state. This should however only be taken as approximate, since neither ground nor excited states are octahedral, although its dominant character justifies our approach. The suggested trend is further confirmed below by the structural analysis of the EXAFS spectrum.

3.3. Molecular Structure from the EXAFS: EXAFS is sensitive to the wave vector of the X-ray generated free photoelectron wave (thus above the IP). Feature C shifts by nearly the same amount as the IP upon oxidation of the central Ru atom. It lies at 3.2 eV above the IP and thus corresponds to a photoelectron wavelength of ca. 6.3 Å (or a photoelectron wave vector $k = 1$ Å^{-1}), which reflects the spatial dimensions of $[Ru^{II}(bpy)_3]^{2+}$. Therefore, the C band should be largely dominated by multiple scattering contributions, also originating from atoms (mostly carbon) beyond the first shell. In fact, a possible additional energy shift of this feature for the excited state lies within the experimental uncertainty, fully in line with the minor structural modifications of the complex on the order of −0.02 Å (see above) for the Ru−N distance.

The D feature, which represents a clear EXAFS modulation, is blue shifted by 1 eV (after correcting for the IP shift), pointing to a bond contraction of the Ru−N nearest-neighbor distance. Note that the energetic shift is considerably smaller than if we had taken the 2.8 eV shift observed in the raw spectra (Table 1 and Figure 3). The capability to precisely measure light-driven energetic shifts in the X-ray domain, as we do here, is a key component to quantify rather small transient structural changes. Natoli et al.[45] laid the theoretical grounds for relating the position of continuum resonances in energy space to the bond lengths within the first coordination shell. They derived a simple relationship, which correlates the energy spacing between the resonance energy E_{res} and the IP to the nearest-neighbor distances R (Ru−N bond distance in our case) via

$$(E_{res} - IP)R_{Ru-N}{}^2 = \text{const} \quad (6)$$

Modifying eq 6 using our measured values for $(E_{res} - IP)$ to calculate the ground (Δ_g) and excited state (Δ_e) energetic difference yields for the relative bond distance changes

$$\Delta R_{Ru-N} = R^{GS}_{Ru-N}\left[\left(\sqrt{\frac{\Delta_g}{\Delta_e}}\right) - 1\right] \quad (7)$$

Equation 6 was already verified[46] as a probe of the first coordination shell distance changes following the energy shifts of the main continuum resonance above the inflection point E_0.[47,48] We have modified this relation to account for the actual energy to generate a propagating photoelectron wave (thus replacing E_0 with IP). With eq 7, we obtain a contraction of the metal−ligand bond distance $\Delta R_{Ru-N} \cong -0.04$ Å, in fair agreement with the above estimate based on the XANES simulation (section 3.2).

Finally, we carried out a full calculation of the ground and excited-state EXAFS using the FEFF 8.20 code (see Supporting Information for details), to the Ru−N bond distances, which were all treated equally (i.e., in D_3 symmetry, see above). Figure 6a and 6b (Figure 6c and 6d) respectively show the ground state (excited state) experimental and optimized EXAFS spectra in q-space and their Fourier transform power spectra (transform magnitudes).

The latter power spectra represent a Pseudo Radial Distribution Function (PRDF, see Supporting Information), which is characterized by a main peak near 1.8 Å and a weaker one near 3.3 Å. The Fourier transform spectra were not phase-corrected for the central atom phase shift; therefore the actual peaks show up at R values shorter than those corresponding to nearest-neighbor atoms. The first peak corresponds to single scattering contributions by the nearest shells of N and C atoms around the Ru atom (N/N′, C2/C2′, and C6/C6′ shown in the inset of Figure 6b), while the second peak is largely due to contributions of more distant shells of atoms (C3/C3′ to C5/C5′), but it also includes complicated multiple scattering paths involving 3 or more atoms in different geometrical arrangements, including collinear multiple scattering paths (the so-called focusing

(43) König, E.; Watson, K. J. *Chem. Phys. Lett.* **1970**, *6*, 457−459.
(44) Hauser, A. *Top. Curr. Chem.* **2004**, *233*, 49−58.
(45) Natoli, C. R.; Benfatto, M.; Doniach, S. *Phys. Rev. A* **1986**, *34*, 4682−4694.
(46) Hodgson, K. O.; Hedman, B.; Penner-Hahn, J. E. *EXAFS and near edge structure III: proceedings of an international conference, Stanford, CA, July 16−20, 1984*; Springer-Verlag: Berlin; New York, 1984.
(47) Bianconi, A.; Fritsch, E.; Calas, G.; Petiau, J. *Phys. Rev. B* **1985**, *32*, 4292−4295.
(48) Lytle, F. W.; Greegor, R. B. *Phys. Rev. B* **1988**, *37*, 1550−1562.

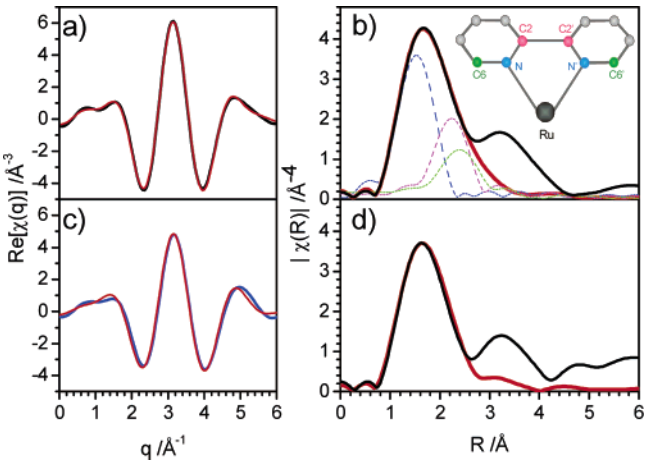

Figure 6. Wave vector spectra and pseudo-radial distribution functions (PRDF) of the ground state (a,b) and the excited state complex (c,d). The black lines represent the experimentally derived traces, while the red ones represent those simulated using the FEFF 8.20 code and the structural parameters from Table 3 (see also Table 2 of the Supporting Information). The PRDFs are decomposed in terms of the various single scattering contributions due to the N, C2, and C6 atoms as seen in the inset (colors correspond between atom and trace), which shows the Ru atom and one bpy ligand. Note that the PRDFs were not phase-corrected for the central atom phase shift, and therefore the actual peaks show up at *R* values shorter than those corresponding to nearest-neighbor atoms (the central atom phase shift can be included in the Fourier transform, and it results in a ca. 0.3−0.5 Å displacement of the radial distribution function).

Table 3. Results of the EXAFS Structural Analysis (Figure 6) for the Ground and the Excited Complex; the Former Is Compared to Crystallographic Data from the Literature

bond	ground state (crystallography)[a]	ground state (EXAFS)	bond change in excited state
Ru−N	2.05−2.064 Å	2.066 ± 0.017 Å	−0.037 ± 0.019 Å

[a] References 56 and 58.

effect[49]). Only the first peak of the PRDF was considered in the EXAFS analysis, as explained in the Supporting Information. Once again, the pseudo-radial distribution function for the excited complex reflects a small contraction with respect to the ground state. The simulated amplitudes of the three dominant single scattering (SS) shells in the 1−2.8 Å range of neighboring N and C atoms are shown, and their sum is compared with the experimental Fourier transform for the ground (Figure 6a) and excited complex (Figure 6d). We derive bond lengths for the ground state and the resulting bond contraction for the excited state that are given in Table 3. The agreement is good between the X-ray crystallography data and the EXAFS-extracted distances for the ground state (Table 3). The uncertainty (±0.019 Å) on the EXAFS data represents a limit for which we observe significant deviations from the measured spectrum. Our result (−0.037 ± 0.019 Å) for the Ru−N bond contraction agrees well with the estimates derived above from eq 5 (−0.02 Å) and eq 7 (−0.04 Å). We also find that all three shells (Ru−N, Ru−C2, and Ru−C6) exhibit a distance decrease from the central atom, compared to the ground-state structure (see Table SII), which shows the consistency of our EXAFS analysis.

To interpret these results, we need to identify the parameters that determine the structure and bonding of the Ru complex. The Ru d-orbitals undergo n-type bonding with the ligand σ-orbitals. In the ground state, the system adopts a nonoctahedral geometry due to the fact that the N−N distance of the bpy ligands is rigid. Under this constraint, the three bpy ligands arrange in a propeller-like geometry around the Ru atom. The coordination of the N atoms is close to octahedral but with deviations, consisting of a compression of the coordination octahedron along the trigonal axis by ∼0.5 Å and a trigonal twisting of ∼10° from the ideal octahedral geometry. In addition to this main bonding contribution, there exists an additional one due to π-back-bonding, resulting from the transfer of electron density from the t_{2g} orbitals to the empty π^*-orbital of the ligand.

Our result of a weak bond contraction by ∼0.03 Å on the average (bearing in mind that we used a D_3 symmetry throughout our analysis), for the excited complex is quite close to earlier X-ray crystallography[22] and solution EXAFS[50] studies showing a bond contraction by ∼0.04 Å between $[Ru^{II}(NH_3)_6]^{2+}$ and $[Ru^{III}(NH_3)_6]^{3+}$. However, crystallographic studies on $[Ru^{II}(bpy)_3]^{2+}$ and $[Ru^{III}(bpy)_3]^{3+}$ [21] concluded to an indistinguishable Ru−N bond distance for the two species. In ref 22, the shortening of the Ru−N bond distances upon oxidation of the Ru−hexamine complex was attributed to polarization effects due to the increased charge on the Ru ion.

In the case of the ground-state complexes $[Ru^{II}(bpy)_3]^{2+}$ and $[Ru^{III}(bpy)_3]^{3+}$, the fact that no change of bond distances was reported upon oxidation of the Ru atom[21] suggests that, despite Ru becoming a stronger electron acceptor, either the reduced π-back-bonding contribution acts against it and/or the geometric constraints hinder the bpy ligand from moving inward. For the excited complex, however, quantum chemical calculations point to a near 100% transfer of charge from the metal to the ligand,[16,35] in agreement with Raman studies of the ^{3}MLCT state,[51] so considerations of donation and back-donation are not operative. A strong electrostatic interaction should occur between the metal atom and the reduced ligand with formation of a dipole and polarization of the uncharged ligands. This will tend to pull the ligands inward, but the fact that the bond contraction is not dramatic points to a steric effect due to straining of the bpy ligands. As mentioned above, these are already constrained in the ground-state geometry due to the rather rigid nature of the N−N distance (itself determined by the C2−C2′ bond distance). Further shortening of the Ru−N bond distances would necessitate a significant structural reorganization of the bpy ligands, which is energetically not possible. Therefore the ligands cannot undergo a significant inward rearrangement in the complex. Hence, we conclude that the mild bond contraction results from electrostatic and polarization forces, which tend to shorten the bond but are limited by steric effects.

One of the consequences of the weak structure rearrangement of the excited complex is on intermolecular electron-transfer processes, which play a role in the transport of excitation and charge in organized assemblies of metal polypyridine complexes[15] and in multicenter polypiridine complexes.[52] The rate of electron transfer between the ground and excited complex

(49) Stern, E. A. In *X-ray absorption principles, applications, techniques of exafs, sexafs and xanes*; Köningsberger, D. C., Prins, R., Eds.; Wiley: New York etc., 1988; pp XII, 673.
(50) Brunschwig, B. S.; Creutz, C.; McCartney, D. H.; Sham, T. K.; Sutin, N. *Faraday Discuss. Chem. Soc.* **1982**, *74*, 113−127.
(51) Webb, M. A.; Knorr, F. J.; McHale, J. L. *J. Raman Spectrosc.* **2001**, *32*, 481−485.
(52) Andersson, J.; Puntoriero, F.; Serroni, S.; Yartsev, A.; Pascher, T.; Polivka, T.; Campagna, S.; Sundstrom, V. *Chem. Phys. Lett.* **2004**, *386*, 336−341.

have, to our knowledge, not been measured, as the species are indistinguishable before and after the process. Our result of a small structural change suggests that electron-transfer processes will be very efficient between them and that, for contact pairs, it is difficult to distinguish from energy transfer. The high rates of 10^9-10^{10} M^{-1} s^{-1} [10,53−55] for energy transfer, leading to charge exchange, point in the same direction, implying a low barrier for electron transfer from one species to the other. This is to relate to the high rates of self-exchange between reduced and oxidized forms of Ru−polypiridine complexes,[5,8] which also suggest little structural reorganization, as pointed out by crystallographic[22,50,56−58] and EXAFS[50] studies.

4. Conclusions

We recorded the X-ray absorption spectra at the L-edges of Ru in the aqueous $[Ru^{II}(bpy)_3]^{2+}$ complex in the ground state and in the excited state, 50 ps up to nanoseconds after photoexcitation with an ultrashort 400 nm laser pulse. The XANES line shapes have been quantitatively simulated with excellent agreement with experiment, using an atomic multiplet code with octahedral and trigonal ligand field contributions, assuming a trigonal symmetry for the excited complex. The analysis of the XANES and of the EXAFS modulations point to a contraction of Ru−N bonds by ∼0.03 Å on the average. This weak bond contraction is discussed in terms of a dominant electrostatic and polarization interaction between the oxidized Ru atom and the neutral and reduced bpy ligands and by steric effects due to straining of the latter. Since the D_3 symmetry was used throughout the modelling of data, it cannot be excluded that the above bond contraction may be the average of several non-equivalent bond contractions. This is however unlikely on the ground of the above mentioned steric effects. The inability of the present data to distinguish between the more probable C_2 symmetry of the excited state and the D_3 symmetry is an inherent limitation of the system and not of the method, since the XANES signatures of the two are identical.

The remarkable quality of the data, in terms of energy resolution and sensitivity to photoinduced changes, and the quantitative spectral shape and structural analysis on the metal−polypyridine complex, show that picosecond and, hopefully soon, femtosecond XAS can be implemented for the study of a large class of photoinduced reactions in coordination chemistry and in biology.[23]

Acknowledgment. This work was supported by the Swiss NSF via Contracts 620-066145 and 2000-67912.02. The experiments were performed at beamline 5.3.1 of the Advanced Light Source. We are grateful to Drs. Alexander Tarnovsky, Maik Kaiser (Lausanne), and Daniel Grolimund (SLS, Villigen). We also thank Drs. S. L. Johnson, P. A. Heimann, and R. W. Schoenlein and Prof. R. Falcone (Berkeley) for their help and assistance during the measurements and Prof. P. Vogel (Lausanne) for useful discussions.

Supporting Information Available: Contains a description of the experimental methods and of the codes used to analyze the XANES line shapes and the EXAFS modulations, along with tables of parameters used in both cases. This material is available free of charge via the Internet at http://pubs.acs.org.

JA054932K

(53) Milosavljevic, B. H.; Thomas, J. K. *J. Phys. Chem.* **1983**, *87*, 616−621.
(54) Shaw, G. B.; Brown, C. L.; Papanikolas, J. M. *J. Phys. Chem. A* **2002**, *106*, 1483−1495.
(55) Ikeda, N.; Yoshimura, A.; Tsushima, M.; Ohno, T. *J. Phys. Chem. A* **2000**, *104*, 6158−6164.
(56) Rillema, D. P.; Jones, D. S.; Levy, H. A. *J. Chem. Soc., Chem. Commun.* **1979**, 849−851.
(57) Bernhard, P.; Bürgi, H. B.; Hauser, J.; Lehmann, H.; Lüdi, A. *Inorg. Chem.* **1982**, *21*, 3936−3941.
(58) Rillema, D. P.; Jones, D. S.; Woods, C.; Levy, H. A. *Inorg. Chem.* **1992**, *31*, 2935−2938.
(59) Desimone, R. E.; Drago, R. S. *J. Am. Chem. Soc.* **1970**, *92*, 2343−2352.